



**HAL**  
open science

# Characterization of resistive Micromegas detectors for the upgrade of the T2K Near Detector Time Projection Chambers

D. Attié, M. Batkiewicz-Kwasniak, P. Billoir, A. Blanchet, A. Blondel, S. Bolognesi, D. Calvet, M.G. Catanesi, M. Cicerchia, G. Cogo, et al.

► **To cite this version:**

D. Attié, M. Batkiewicz-Kwasniak, P. Billoir, A. Blanchet, A. Blondel, et al.. Characterization of resistive Micromegas detectors for the upgrade of the T2K Near Detector Time Projection Chambers. Nuclear Instruments and Methods in Physics Research Section A: Accelerators, Spectrometers, Detectors and Associated Equipment, 2022, 1025, pp.166109. 10.1016/j.nima.2021.166109 . hal-03284461

**HAL Id: hal-03284461**

**<https://hal.science/hal-03284461>**

Submitted on 8 Jan 2024

**HAL** is a multi-disciplinary open access archive for the deposit and dissemination of scientific research documents, whether they are published or not. The documents may come from teaching and research institutions in France or abroad, or from public or private research centers.

L'archive ouverte pluridisciplinaire **HAL**, est destinée au dépôt et à la diffusion de documents scientifiques de niveau recherche, publiés ou non, émanant des établissements d'enseignement et de recherche français ou étrangers, des laboratoires publics ou privés.



Distributed under a Creative Commons Attribution - NonCommercial 4.0 International License

# Characterization of resistive Micromegas detectors for the upgrade of the T2K Near Detector Time Projection Chambers

D. Attié<sup>a</sup>, M. Batkiewicz-Kwasniak<sup>b</sup>, P. Billoir<sup>c</sup>, A. Blanchet<sup>c</sup>, A. Blondel<sup>c</sup>, S. Bolognesi<sup>a</sup>, D. Calvet<sup>a</sup>, M.G. Catanesi<sup>d</sup>, M. Cicerchia<sup>e</sup>, G. Cogo<sup>f</sup>, P. Colas<sup>a</sup>, G. Collazuol<sup>f</sup>, A. Delbart<sup>a</sup>, J. Dumarchez<sup>c</sup>, S. Emery-Schrenk<sup>a</sup>, M. Feltre<sup>f</sup>, C. Giganti<sup>c</sup>, F. Gramegna<sup>e</sup>, M. Grassi<sup>f</sup>, M. Guigue<sup>c</sup>, P. Hamacher-Baumann<sup>g</sup>, S. Hassani<sup>a,1</sup>, F. Iacob<sup>f</sup>, C. Jesús-Valls<sup>h</sup>, R. Kurjata<sup>i</sup>, M. Lamoureux<sup>f</sup>, M. Lehuraux<sup>a</sup>, A. Longhin<sup>f</sup>, T. Lux<sup>h</sup>, L. Magaletti<sup>d</sup>, T. Marchi<sup>e</sup>, A. Maurel<sup>a</sup>, L. Mellet<sup>c</sup>, M. Mezzetto<sup>f</sup>, L. Munteanu<sup>a</sup>, Q. V. Nguyen<sup>c</sup>, Y. Orain<sup>c</sup>, M. Parif<sup>f</sup>, J.-M. Parraud<sup>c</sup>, C. Pastore<sup>d</sup>, A. Pepato<sup>f</sup>, E. Pierre<sup>c</sup>, B. Popov<sup>c</sup>, H. Przybiliski<sup>b</sup>, T. Radermacher<sup>g</sup>, E. Radicioni<sup>d</sup>, M. Riallot<sup>a</sup>, S. Roth<sup>g</sup>, A. Rychter<sup>i</sup>, L. Scomparin<sup>f</sup>, J. Steinmann<sup>g</sup>, S. Suvorov<sup>c,j,2</sup>, J. Swierblewski<sup>b</sup>, D. Terront<sup>c</sup>, N. Thamm<sup>g</sup>, F. Toussnel<sup>c</sup>, V. Valentino<sup>d</sup>, G. Vasseur<sup>a</sup>, U. Yevarouskaya<sup>c</sup>, M. Ziembicki<sup>i</sup>, M. Zito<sup>c</sup>

<sup>a</sup>IRFU, CEA, Université Paris-Saclay, Gif-sur-Yvette, France

<sup>b</sup>H. Niewodniczanski Institute of Nuclear Physics PAN, Cracow, Poland

<sup>c</sup>LPNHE, Sorbonne Université, Université de Paris, CNRS/IN2P3, Paris, France

<sup>d</sup>INFN sezione di Bari, Università di Bari e Politecnico di Bari, Italy

<sup>e</sup>INFN: Laboratori Nazionali di Legnaro (LNL), Padova, Italy

<sup>f</sup>INFN Sezione di Padova and Università di Padova, Dipartimento di Fisica e Astronomia, Padova, Italy

<sup>g</sup>RWTH Aachen University, III. Physikalisches Institut, Aachen, Germany

<sup>h</sup>Institut de Física d'Altes Energies (IFAE), The Barcelona Institute of Science and Technology, Bellaterra, Spain

<sup>i</sup>Warsaw University of technology, Warsaw, Poland

<sup>j</sup>Institute for Nuclear Research of the Russian Academy of Sciences, Moscow, Russia

---

## Abstract

---

\*Corresponding author

<sup>1</sup>samira.hassani@cea.fr

<sup>2</sup>sergey.suvorov@lpnhe.in2p3.fr

Preprint submitted to Nuclear Instruments and Methods

October 28, 2021

The second phase of the T2K experiment is expected to start data taking in autumn 2022. An upgrade of the Near Detector (ND280) is under development and includes the construction of two new Time Projection Chambers called High-Angle TPC (HA-TPC). The two endplates of these TPCs will be paved with eight Micromegas type charge readout modules. The Micromegas detector charge amplification structure uses a resistive anode to spread the charges over several pads to improve the space point resolution. This innovative technique is combined with the bulk-Micromegas technology to compose the "Encapsulated Resistive Anode Micromegas" detector. A prototype has been designed, built and exposed to an electron beam at the DESY II test beam facility.

The data have been used to characterize the charge spreading and to produce its map. Spatial resolution better than 600  $\mu\text{m}$  and energy resolution better than 9% are obtained for all incident angles. These performances fulfil the requirements for the upgrade of the ND280 TPC.

*Keywords:* Resistive Micromegas, T2K Near Detector Time Projection Chambers

---

1	<b>Contents</b>	
2	<b>1 Introduction</b>	<b>4</b>
3	<b>2 Resistive Micromegas</b>	<b>6</b>
4	<b>3 Experimental setup</b>	<b>8</b>
5	<b>4 Collected data</b>	<b>10</b>
6	<b>5 Charge spreading characterisation</b>	<b>10</b>
7	<b>6 Pattern recognition</b>	<b>13</b>
8	<b>7 Spatial resolution</b>	<b>13</b>
9	7.1 The Pad Response Function method . . . . .	14
10	7.2 Spatial resolution estimation . . . . .	15
11	7.3 Spatial resolution dependence on the drift distance, momen-	
12	tum, high voltage . . . . .	16
13	7.4 Spatial resolution dependence on the track inclination . . . . .	17

14	7.5	Bias measurements . . . . .	19
15	<b>8</b>	<b>Deposited energy resolution</b>	<b>20</b>
16	8.1	Definition of the cluster charge . . . . .	22
17	8.2	Deposited energy resolution for inclined tracks . . . . .	23
18	8.3	Dependence of the $dE/dx$ resolution on the number of clusters	26
19	<b>9</b>	<b>RC map calculation</b>	<b>27</b>
20	<b>10</b>	<b>Conclusions</b>	<b>30</b>

## 21 1. Introduction

22 T2K [1] is a long-baseline neutrino oscillation experiment exploiting a  
23 muon neutrino beam produced by the JPARC accelerator complex in Japan.  
24 The T2K experiment includes the secondary neutrino beamline, a set of near  
25 detectors (INGRID and ND280) and the far detector SuperKamiokande.

26 T2K provided the first evidence of non-zero mixing angle  $\theta_{13}$  [2] and dis-  
27 covered the appearance of electron neutrinos in a muon neutrino beam [2, 3,  
28 4]. Combining T2K data with precise  $\theta_{13}$  measurement from reactor experi-  
29 ments, T2K has recently reported hints of large Charge-Parity (CP) violation  
30 in the leptonic sector [5], excluding CP-conservation at about the  $2\sigma$  Confi-  
31 dence Level.

32 The T2K collaboration is now preparing for the second phase of the ex-  
33 periment (T2K-II), starting in Fall 2022, which will exploit the upgrade of  
34 the beam from 500 kW to 750 kW. T2K-II will collect in total more than  $10^{22}$   
35 Protons-On-Target (POT), including the  $3.6 \times 10^{21}$  POT already collected,  
36 thus enabling  $3\sigma$  sensitivity on CP-Violation, in case of maximally violated  
37 CP, as currently indicated by the T2K results [5]. In order to cope with such  
38 increased statistics, improved control of the relevant systematic uncertainties  
39 is needed. To this aim, an upgrade to ND280 is being constructed.

40 ND280 is a magnetized multi-purpose detector that measures, before the  
41 oscillation, the neutrino differential rate versus the kinematics variables of  
42 the particles, mostly muons, that result from the neutrino interaction with  
43 nuclei in dense parts of the detector. This allows one to constrain the neu-  
44 trino flux and the neutrino-nucleus interaction cross-section. The present  
45 ND280 consists of two main parts: an upstream  $\pi^0$  detector (P0D) and a  
46 downstream tracker which includes two Fine Grained Scintillators (FGD) in-  
47 terleaved with three vertical Time Projection Chambers (TPCs). The P0D  
48 and the tracker are surrounded by an electromagnetic calorimeter (ECAL)  
49 and by the UA1 magnet providing a 0.2 T magnetic field. The magnet yoke  
50 is further instrumented with a Side Muon Range Detector (SMRD).

51 The role of ND280 in the T2K oscillation analysis is crucial, allowing one  
52 to constrain the uncertainty on the expected number of events at the far  
53 detector to 4-5%. ND280 measurements are performed on different targets  
54 (Carbon and Oxygen) and rely on the precise measurement of the muon  
55 momentum measured by the TPCs, with a momentum resolution of 10%  
56 at 1 GeV [6]. Better resolution is not needed since the determination of  
57 the incoming neutrino energy from the outgoing muon momentum in  $\nu_\mu$

58 charged-current interactions are limited by the uncertainty induced by the  
59 Fermi motion of the nucleon in the nucleus.

60 Another important result of ND280 is the measurement of the  $\nu_e$  con-  
61 tamination in the beam [7, 8], which constitutes one of the two main back-  
62 grounds to the  $\nu_e$  appearance in the electron-like sample selected at Super-  
63 Kamiokande. This analysis, based on the Particle Identification (PID) capa-  
64 bilities of the TPCs and of ECAL, is possible thanks to the deposited energy  
65 resolution of 8% in the TPCs that allows sufficient e- $\mu$  separation between a  
66 few hundred MeV and  $\sim 2$  GeV.

67 The upgrade of ND280 consists in substituting the P0D with a new  
68 tracker, similar to the existent one but with a horizontal orientation parallel  
69 to the neutrino beam, and able to detect particles transverse to the beam,  
70 for which the acceptance of the current tracker is small. The new tracker  
71 includes a 3-dimensional scintillator target for neutrino interactions(Super-  
72 FGD) made of about 2 million 1 cm<sup>3</sup> cubes, read out by wavelength shifting  
73 fibers in the 3 directions [9]. On the top and the bottom of the Super-FGD,  
74 two High-Angle TPCs (HA-TPCs) will be installed. The new tracker system  
75 will be surrounded by six Time-of-Flight modules. This new detector con-  
76 figuration will allow one to improve the angular acceptance of ND280, being  
77 close to the full  $4\pi$  phase-space accessible at SuperKamiokande. In addition,  
78 the better tracking performances of the super-FGD will allow improving the  
79 reconstruction of the hadronic part of the neutrino interactions, which will  
80 be exploited in combination with the muon kinematics. Also, more target  
81 mass for neutrino interactions yields more data statistics.

82 Each endplate of the new TPCs will be instrumented with eight Mi-  
83 cromegas type charge readout modules. The Micromegas detector charge  
84 amplification structure uses a resistive anode to "spread" the charges over  
85 several pads to improve the space point resolution: a signal is induced in pads  
86 adjacent to the pad receiving directly electrons from the avalanche, and the  
87 information from those additional signals allows one to better measure the  
88 track position. This effect is different from the charge sharing between pads  
89 resulting from the diffusion of the primary electrons in the TPC gas. This  
90 innovative technique is combined with the bulk-Micromegas technology [6]  
91 to compose the "Encapsulated Resistive Anode Micromegas" (ERAM) de-  
92 tector. Performances of a prototype of an ERAM detector exposed to a test  
93 beam at CERN were shown in [10]. This paper describes the performance  
94 of one prototype ERAM module, built with the same design that will be  
95 used for the HA-TPCs, exposed to an electron beam at DESY. With respect

96 to our previous studies reported in [10], in this paper we characterize both  
97 spatial and  $dE/dx$  resolution as a function of the angle of the track projec-  
98 tion reconstructed in the ERAM plane, with the side of the ERAM plane,  
99 corresponding to the sides of the ERAM pads.

100 The HA-TPC should match the performance of existing TPCs in terms  
101 of momentum and  $dE/dx$  resolution. In addition, the super-FGD will enable  
102 the reconstruction of low momentum protons and neutrons [11], thus allowing  
103 one to reconstruct the incoming neutrino energy more precisely and *effectively*  
104 correct for the Fermi motion: an improved track momentum resolution in  
105 the HA-TPC, even beyond the previous specifications, is therefore useful  
106 to improve the neutrino energy resolution and, ultimately, the precision on  
107 neutrino oscillation measurements.

## 108 2. Resistive Micromegas

109 The ERAM detector uses the bulk-Micromegas technology invented in  
110 2004 by a collaboration between the CERN/EP-DT-EF PCB workshop and  
111 CEA-IRFU [12]. It was developed and used for the construction of the 72  
112 bulk-Micromegas modules ( $9\text{ m}^2$  total area) which equip the three T2K/ND280  
113 vertical TPCs. The woven micromesh of the Micromegas detector is sand-  
114 wичed between two layers of the same insulating material (pyralux) and  
115 exposed to UV radiation at the location where the pyralux is kept on top of  
116 the pad-segmented anode PCB after chemical development.

117 The ERAM detector is a  $128\text{ }\mu\text{m}$  amplification gap bulk-Micromegas using  
118 the standard SD45/18 304L woven micromesh built on top of a resistive anode  
119 PCB. When a charged particle crosses the gas volume of a TPC, it generates  
120 a cloud of ionized electrons. These electrons are drifted to the anode readout  
121 plane of the TPC under a uniform electric field. On the readout plane, an  
122 avalanche is generated by a high electric field in the Micromegas amplification  
123 region. The voltage that induced this field is notated as “DLC voltage” in  
124 the following of this paper. The DLC layer is powered at High Voltage on  
125 each of the 4 sides through the DLC-covered kapton foil. The 3D position  
126 of the track is then reconstructed from the arrival time and the position of  
127 the avalanche on the readout plane. In the case of the bulk-Micromegas, the  
128 electron avalanche in the amplification gap is much smaller comparing to the  
129 pad size ( $\approx 1\text{ cm}$ ) and therefore the position resolution is often limited by the  
130 pad size. The resistive anode Micromegas, first introduced and extensively  
131 studied by the ILC-TPC collaboration [13], provides a way to induce a signal

132 on a larger number of pads allowing for a better reconstruction of the track  
 133 position. A sketch of the bulk and the resistive Micromegas concepts are  
 134 presented in Figure 1.

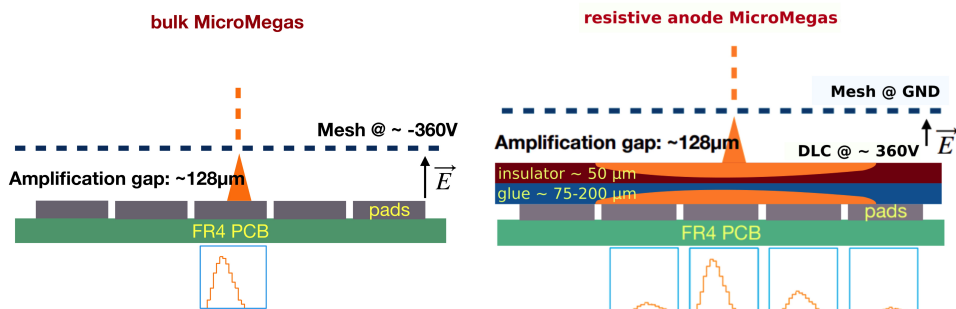


Figure 1: A sketch of the Standard Bulk Micromegas layout (left) and the Resistive anode Micromegas layout (right).

135 The anode, segmented in pads, is covered by a foil of insulating material,  
 136 which has a thin resistive layer on its top side. The ERAM detector uses a  
 137 Diamond-Like Carbon (DLC) thin layer sputtered on a 50 µm thick APICAL  
 138 (Kapton) insulator sheet. The avalanche is then naturally quenched because  
 139 the potential difference locally drops in presence of a high charge density.  
 140 The resistive layer effect can be approximated with a 2-D RC network. The  
 141 charge deposited by the avalanche induces a signal also on the adjacent pads.  
 142 Within the RC model the charge spread is following a Gaussian distribution.  
 143 For a point charge deposited at  $r = 0$  and  $t = 0$ , the charge density as a  
 144 function of radius  $r$  and time  $t$  is given by:

$$\rho(r, t) = \frac{RC}{4\pi t} e^{-\frac{r^2 RC}{4t}} \quad (1)$$

145 where  $R$  is the resistivity per unit area and  $C$  is the capacitance per unit  
 146 area. For this structure, the capacitance  $C$  is defined by the distance between  
 147 the resistive layer and the grounded pads (glue thickness plus APICAL foil).  
 148 These characteristics determines the width of the induced charge spread  $\sigma_t$   
 149 at a given time. When measured, due to integration of the charge collected  
 150 by a front-end electronics of shaping time  $t$ , this spread is of the order of  
 151  $\sigma_t = \sqrt{\frac{2t}{RC}}$ .

152 The resistive anode provides mainly two advantages: by spreading the  
 153 charge between neighbouring pads, it improves greatly the resolution with



154 respect to the pitch/ $\sqrt{12}$  provided by a mere hodoscope, and it suppresses  
155 the formation of sparks and limits their intensity. The first one is the main  
156 advantage in the context of the T2K experiment. A further and novel im-  
157 provement of this technique is a new High Voltage powering scheme, where  
158 the mesh is set to ground and the anode to a positive amplification volt-  
159 age. The insulation of the resistive anode from the pads, hence from the  
160 electronics, ensures a safe operation by a capacitive coupling readout and  
161 thus allows us to remove the cumbersome anti-spark protection circuitry of  
162 electronic read-out boards necessary in the case of the standard bulk readout.

163 At the end of 2017, the first series of prototypes were produced and  
164 tested to assess the feasibility of large charge spreading by a low resistivity  
165 anode. The vertical TPCs PCB, with an active area of  $36 \times 34$  cm<sup>2</sup> covered  
166 by  $0.97 \times 0.69$  cm<sup>2</sup> pads, was adapted to build an ERAM structure with "on-  
167 shelf" 2.5 MOhm/ $\square$  DLC foils. This first prototype was tested with a particle  
168 beam at CERN in 2018 and its performances are summarized in [10].

169 In fall 2018, the global design of the ND280 upgrade detector was fixed.  
170 The sub-detector envelopes were defined and the size of the ERAM modules  
171 fixed to be  $420 \times 340$  mm<sup>2</sup> with  $32 \times 36$  rectangular pads of size  $10.09 \times$   
172  $11.18$  mm<sup>2</sup>. The ERAM module studied in this paper has a resistivity close  
173 to the required one of 200 kOhm/ $\square$  using DLC foils stack on a 75  $\mu$ m glue  
174 layer. The resistivity maps measured at critical steps of the manufacturing  
175 of the DLC foil shows a non-uniformity of 20%. The detector is readout  
176 with two analogue 576 channels AFTER based Front-End Cards (eight 72  
177 channels AFTER ASIC per card). The AFTER chip, already used for the  
178 existing TPCs of T2K and for the test beam described in [10] allows tuning  
179 several parameters such as the gain, the shaping time and the sampling time.  
180 This prototype was tested in a test beam at DESY in June 2019.

### 181 **3. Experimental setup**

182 The prototype has been exposed to an electron beam at the DESY II  
183 test beam facility [14]. DESY II provides electron beams of 1 – 6 GeV/c  
184 at a rate of up to several kHz, depending on the chosen momentum. In  
185 the test beam area TB24/1, a large-bore superconducting solenoid, called  
186 PCMAG, provides a magnetic field of up to 1.25 T. The magnet is mounted  
187 on a movable platform, which allows the setup to be moved horizontally and  
188 vertically, perpendicular to the beam line, as well as rotated by  $\pm 45^\circ$  in the  
189 horizontal plane. The platform can position the device under test with a

190 precision of about 0.2 mm horizontally, 0.1 mm vertically, and within  $0.1^\circ$  in  
191 angle.

192 Inside the bore of the magnet, a rail system is installed on which test  
193 devices can be mounted at different positions within the magnet. The TPC  
194 prototype is supported on a sled, which can move in and out of the magnet  
195 and can be used to rotate the chamber around the magnetic field axis as  
196 illustrated in Figure 2.

197 Usually, the magnet is positioned perpendicular to the beam, so the mag-  
198 netic field is also perpendicular to the beam, in a horizontal plane. The  
199 ERAM module is a vertical plane parallel to the beam, but perpendicular to  
200 the magnetic field. The walls of the magnet present about 20 % of a radiation  
201 length, so that an electron beam of 6 GeV/c easily penetrates the magnet  
202 and the device under test. A set of four consecutive scintillation counters, of  
203 which each has an area of approximately  $2.5 \text{ cm} \times 2.5 \text{ cm}$ , is mounted about  
204 1.5 m in front of the magnet. The coincidence between them is used as a  
205 beam trigger. In addition, a second set of scintillation counters above and  
206 below the magnet provides a cosmic trigger for tests without beam.

207 The prototype has been placed inside the magnetic field of 0.2 T provided  
208 by the PCMAG magnet and has been operated for these measurements with  
209 a gas mixture of 95% argon, 3% tetrafluoromethane ( $\text{CF}_4$ ), and 2% isobutane  
210 ( $\text{iC}_4\text{H}_{10}$ ) that is the same gas mixture as the one used in the existing TPCs  
211 of ND280. The gas quality was constantly monitored during the measure-  
212 ment. For the results reported in this paper, the oxygen contamination was  
213 around 30 ppm at a gas flow rate of  $30 \text{ l/h}$ . The chamber was operated at  
214 atmospheric pressure. Ambient temperature and pressure were constantly  
215 monitored.

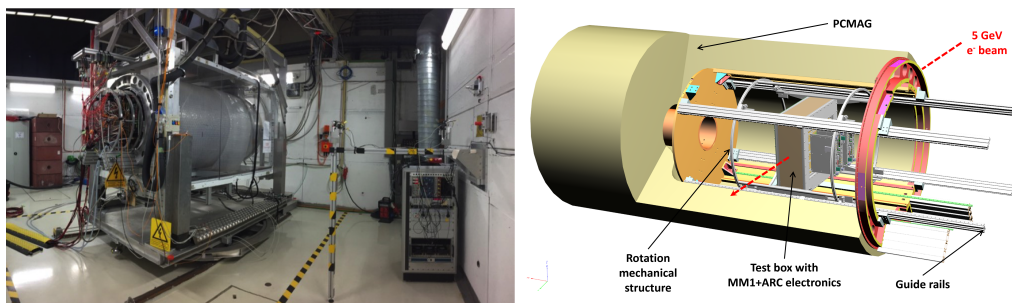


Figure 2: View of the setup.

## 216 4. Collected data

217 The collected data are used to analyze in detail the role of all the relevant  
218 parameters (electronics peaking time, DLC voltage, drift distance) to fully  
219 characterize the charge spreading, the resistive foil uniformity, and to ensure a  
220 performance satisfying the ND280 upgrade requirements. The tests at DESY  
221 were done in a short chamber with a 15 cm drift distance. The prototype was  
222 operated with a DLC voltage of 360 V. The settings chosen for the AFTER  
223 chip were a sampling time of 40 ns, a peaking time of 412 ns or 200 ns,  
224 and a ADC capacitance of 120 fC. The zero-suppression was applied with  
225 measuring the noise individually per pad and the  $5\sigma$  threshold was set based  
226 on the noise fluctuations.

227 The results presented in this paper were obtained with electrons with  
228 momenta varying from 0.5 to 5 GeV/c. We have carried out drift distance  
229 scans with seven points, spaced by 2 cm, at  $B = 0$  T and  $B = 0.2$  T, peaking  
230 time of 200 ns or 412 ns, and DLC voltage of 370 V and 360 V. In addition  
231 a scan of the DLC voltage, varied from 330 V to 400 V, was performed.

232 We have calibrated the Micromegas position with respect to the magnet  
233 frame coordinate system, the moving table position, and the drift velocities  
234 at different drift fields with a 4 GeV/c electron beam and a short peaking  
235 time of 116 ns. At the standard T2K drift field of 275 V/cm, we obtained a  
236 drift velocity of  $7.68 \pm 0.03$  cm/ $\mu$ s by drift distance scans with the accelerator  
237 beam. A Gas Monitoring Chamber (GMC), identical to the ones deployed  
238 at T2K's ND280 detector [6], monitored the exhaust gas for the duration of  
239 the beam-time. The GMC measured a drift velocity of  $7.81 \pm 0.02$  cm/ $\mu$ s at  
240 the T2K field, in agreement with the beam scans, see Figure 3. Under the  
241 electric field of 140 V/cm, which is associated with the minimum transverse  
242 diffusion, we found a drift velocity of 5.84 cm/ $\mu$ s. Despite the impact of the  
243 gas bottle changes on the gas properties, the drift velocity  $V_{\text{drift}}$  under the  
244 electric field of  $E = 275$  V/cm varies less than 6‰.

## 245 5. Charge spreading characterisation

246 As explained before, the resistive Micromegas technology produces a  
247 spreading of the collected charge into neighbouring pads. The charge spread-  
248 ing phenomenon, which drives the waveform shape in the pads, is described  
249 in [13]. The signal in the adjacent pads is smaller in amplitude, delayed and  
250 longer in time compared to the signal in the leading pad where the avalanche

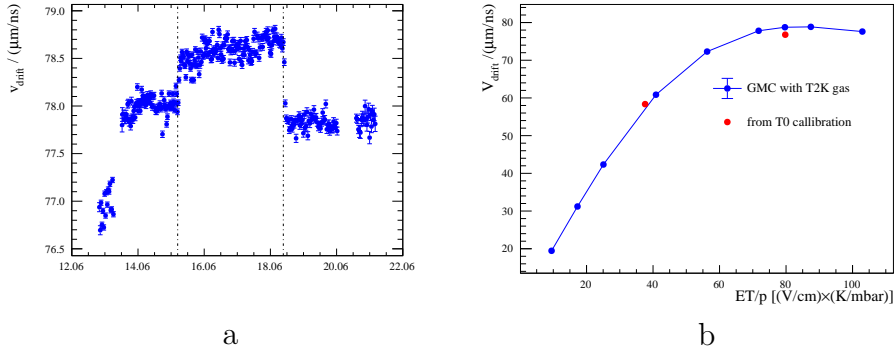


Figure 3: The drift velocity under a constant field of 275 V/cm as a function of date (a) and as a function of electric field (b) with density corrections applied. The vertical lines on (a) correspond to the moments when the bottles of premixed gas were replaced. Transition regions at ramp-up and between bottle changes can be seen. The measurements at different fields in (b) correspond to a full day during the first bottle (14.06).

251 is located. The time delay of the waveform increases with the distance of the  
 252 adjacent pad to the track. To study the phenomenon of interest, we define a  
 253 “cluster” as a group of pads in the perpendicular direction to the track. A  
 254 schematic view of such a cluster for horizontal tracks and waveforms in the  
 255 leading and in adjacent pads are shown in Figure 4.

256 In the current work, the maximum of the waveform is used as an estimator  
 257 of the charge in each pad, which corresponds to different times for the leading  
 258 and adjacent pads. In Figure 5, the pad multiplicity per cluster and the ratio  
 259 of the charge measured in the pad with the largest signal with respect to the  
 260 sum of the charges of the pads in the cluster ( $q_{\text{max}}/q_{\text{cluster}}$ ) are shown. The  
 261 other possible approaches e.g. fit of the waveform with an analytical function  
 262 are under study.

263 Most of the clusters are formed by more than two pads and the pad with  
 264 the largest signal contains typically 80% of the total charge of the cluster. The  
 265 effect of the high voltage on the multiplicity is also clearly seen in Figure 5.  
 266 The cluster multiplicity increases with the high voltage, as the probability  
 267 for the smaller signals in some pads to pass the threshold increases with the  
 268 gain.

269 For tracks projections in the pad plane which are parallel to the sides of  
 270 the pads, transverse spreading is defined precisely within the given column.  
 271 While for inclined tracks and large square pads, the separation between lon-  
 272 gitudinal (along the track) and transverse spreading is more complicated. In

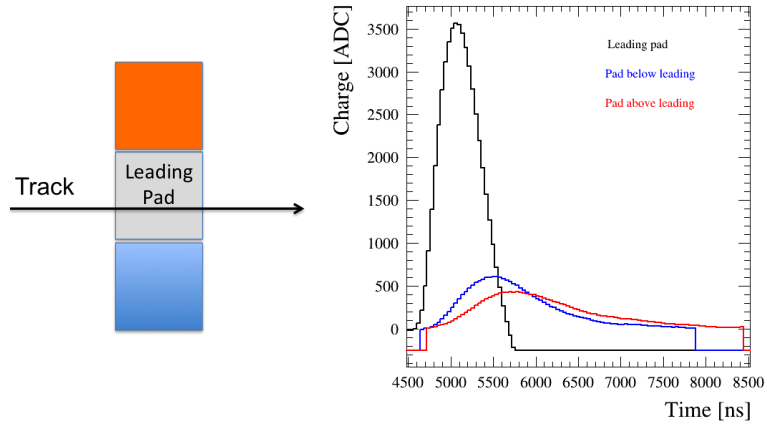


Figure 4: A schematic view of a column cluster (left) and the waveforms of each pad composing this cluster (right) for 412 ns shaping time.

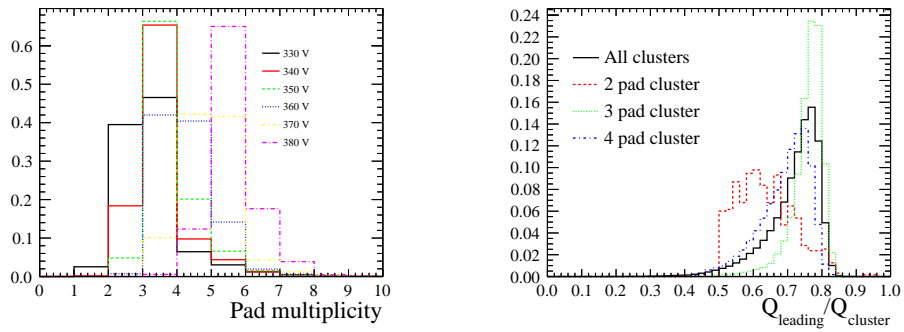


Figure 5: The number of pads in a cluster versus the DLC high voltage (left) and the fraction of the cluster charge collected in the pad with largest signal at 360 V (right).

273 order to distinguish these two spreading topologies, we define more sophis-  
 274 ticated cluster patterns shown in Figure 6. These clusters are repeated to  
 275 pave the whole ERAM. In the case of square pads, these patterns are optimal  
 276 for angles with tangents 0 (column), 1 (diagonal), 0.5 (2 by 1), 0.3 (3 by 1)  
 277 respectively. In the case of rectangular pads, the optimal angles are slightly  
 278 different.

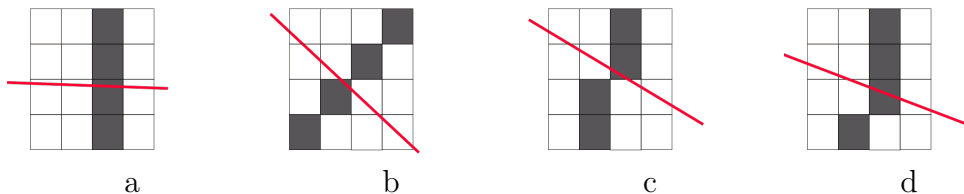


Figure 6: The different cluster patterns that can be used depending on the track (red line) angle with the pads sides : (a) column, (b) diagonal, (c) 2 by 1, (d) 3 by 1. For each case, the colored pads correspond to one cluster, associated to the colored leading pad crossed by the track.

## 279 6. Pattern recognition

280 In the test beam analysis, we focus on the studies of tracks crossing  
 281 the whole detector as more complicated typologies (e.g. showering, curved  
 282 low-energy tracks) are difficult to interpret. Hence simple reconstruction  
 283 algorithms like DBSCAN [15] are sufficient in our case.

284 We select a track if it is crossing the whole detector without breaks or  
 285 splits. A split is defined as the case where there is more than one cluster in a  
 286 given column. An event containing a split is thus a multiple track candidate  
 287 and is rejected in our analysis. However, with the resistive spreading, two  
 288 close parallel tracks may not be separated by a gap and thus misreconstructed  
 289 as one single track. To reject such a topology, a cut on the pad multiplicity  
 290 in each cluster was implemented. The cut value was optimised for each  
 291 Micromegas voltage and electronics shaping time. Examples of the accepted  
 292 and rejected events are shown in Figure 7 (a) and (b) respectively.

## 293 7. Spatial resolution

294 As described in section 1, the momentum resolution has to be better than  
 295 10% at 1 GeV/c but, to fully exploit the ND280 upgrade capabilities, even

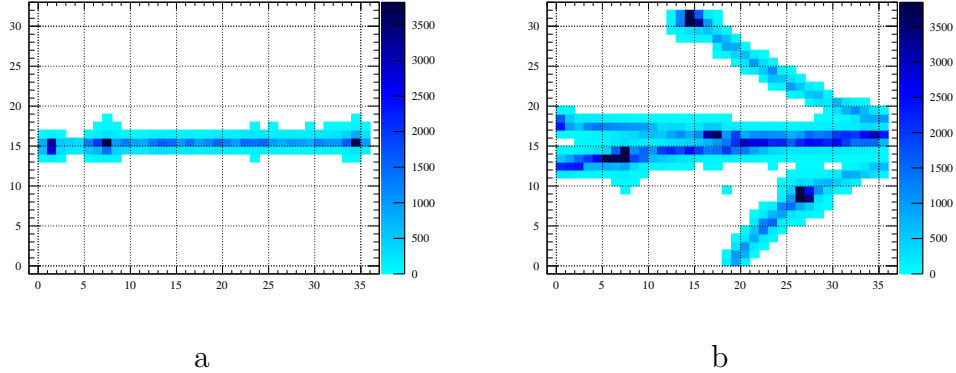


Figure 7: Event displays of the (a) single track and (b) multi-track in the prototype.

296 better momentum resolution would be desirable. The momentum resolution  
 297 is directly connected to the spatial resolution obtained for one cluster through  
 298 the Gluckstern formula [16]. For tracks with 70 point measurements (using  
 299 clusters), a maximum drift distance of 1 m, and a magnetic field of 0.2 T,  
 300 a spatial resolution of  $\sim 800\mu\text{m}$  would be sufficient to reach a momentum  
 301 resolution of 10% at 1 GeV/c.

302 As we will show in this section, the resistive Micromegas technology allows  
 303 one to significantly improve the spatial resolution with respect to the bulk  
 304 Micromegas, even in presence of slightly larger pads thus allowing one to  
 305 reduce by  $\sim 30\%$  the total number of electronic channels for the same active  
 306 surface. The test beam data have been used to characterize the ERAM  
 307 module performances for electrons with different angles with the pads sides.

### 308 7.1. The Pad Response Function method

309 The charge spread described in the section 5 results in charge detection  
 310 in a few pads around the avalanche arrival point. The maximal charge of the  
 311 waveform signal induced in the adjacent pads is related to the initial charge  
 312 on the leading pad, in a very different way from the one that would result  
 313 from a direct charge sharing on the pads, for example due to the diffusion  
 314 in the TPC gas. That is why the barycentric method is not an optimized  
 315 estimator of the position reconstruction. The dependence of the induced  
 316 maximal signal in the adjacent pads versus the initial charge depends mostly  
 317 on the charge spreading in the Micromegas module but also on other effects  
 318 like the diffusion in the TPC gas, the electronics response, the integration

319 of the charge over the pad surface area etc. The data allow to measure  
 320 and calibrate the resulting dependence using the so-called Pad Response  
 321 Function approach. The Pad Response Function (PRF) which characterizes  
 322 the relation between observed charge ratios and track position with respect to  
 323 the pad (Equation 2). This method improves the spatial resolution compared  
 324 to the barycentric method for TPCs with the resistive anode [17]. The PRF  
 325 is defined as:

$$PRF(x_{track} - x_{pad}) = Q_{pad}/Q_{cluster} \quad (2)$$

326 where  $x_{track}$  is the reconstructed position of the track,  $x_{pad}$  is the centre of  
 327 the pad,  $Q_{pad}$  is the charge collected on a given pad and  $Q_{cluster}$  is the charge  
 328 collected on the whole cluster. The definition of the cluster is the same as  
 329 described in section 5: it's a group of pads where one receives a charge from  
 330 the initial avalanche and the others detect the charge spread in the resistive  
 331 foil.

332 To parametrize the PRF we used the empirical ratio of two symmetric  
 333 4<sup>th</sup> order polynomials proposed in [18]:

$$PRF(x, \Gamma, \Delta, a, b) = A \times \frac{1 + a_2x^2 + a_4x^4}{1 + b_2x^2 + b_4x^4} \quad (3)$$

334 where the parameters  $a_i$  and  $b_i$  can be related to the more physical parame-  
 335 ters: the full width at half maximum  $\Gamma$ , the base width  $\Delta$ , and two scaling  
 336 parameters  $a$  and  $b$ .

### 337 7.2. Spatial resolution estimation

338 This parametrized function of the PRF allows one to determine the pa-  
 339 rameters using an iterative method. To get a first guess of the PRF parame-  
 340 ters, we use the track position reconstruction obtained from the barycentric  
 341 method. After having defined the position of all the clusters, the global track  
 342 is fit with a 2 degree polynomial function. The fit is based on many measure-  
 343 ments using the different clusters along the track ( $\geq 34$ ) thus it is considered  
 344 as a true track position and the PRF scatter plot is filled (Figure 8 (a)). The  
 345 scatter plot is profiled along Y axis to form a graph that is further fit with  
 346 the analytical function from Equation 3 (Figure 8 (b)).

347 After having determined the PRF, the track position in each cluster is



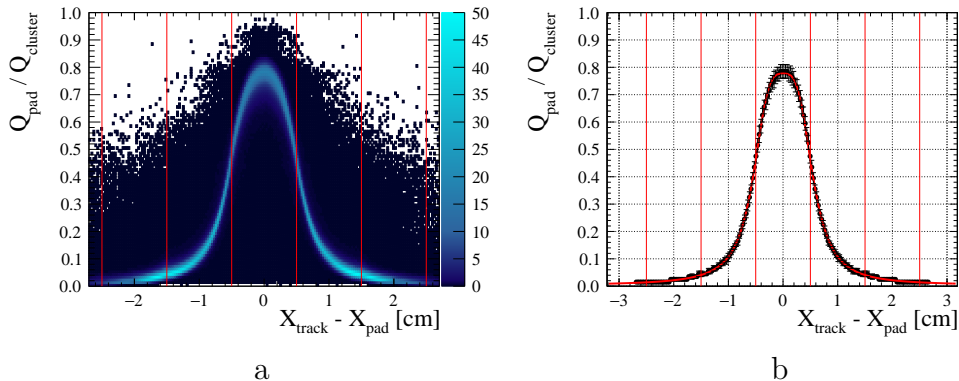


Figure 8: The Pad Response Function (PRF) obtained with (a) scatter plot and (b) results of its profile and fit with analytical function. The pad borders are represented by vertical lines.

348 obtained with the following  $\chi^2$  minimization:

$$\chi^2 = \sum_{pads} \frac{Q_{pad}/Q_{cluster} - PRF(x_{track} - x_{pad})}{\sigma_{Q_{pad}/Q_{cluster}}} \quad (4)$$

349 where  $\sigma_Q$  is the uncertainty on the charge measurements. In our analysis, we  
 350 assume that charge measurement probability follows a Poisson distribution,  
 351 hence:  $\sigma_{Q_{pad}/Q_{cluster}} = \sqrt{Q_{pad}/Q_{cluster}}$ . We proceed through the iterative  
 352 process of the PRF estimation until the track fit quality is not improving  
 353 anymore. Typically this procedure converges after few iterations and for the  
 354 results shown in this paper 10 iterations were used.

355 The spatial resolution is defined as the difference between the recon-  
 356 structed position in a given cluster and the track global fit (residual). The  
 357 particular cluster where the resolution is studied is excluded from the fit to  
 358 prevent biases. The residuals distribution is fit with a Gaussian function  
 359 whose standard deviation defines the spatial resolution.

### 360 7.3. Spatial resolution dependence on the drift distance, momentum, high 361 voltage

362 The spatial resolution was studied with different samples. The beam  
 363 position was varied within the drift distance of the field cage keeping the  
 364 tracks parallel to the Micromegas plane. For resistive Micromegas, the spatial  
 365 resolution is expected to degrade slightly for a larger drift distance affected

366 by the transverse and longitudinal diffusion. The observed dependence, for  
 367 a DLC voltage of 360 V, is shown in Figure 9 (a). A resolution between 200  
 368 and 250  $\mu\text{m}$  is observed for the whole drift length.

369 In addition, the high voltage applied to the Micromegas mesh was varied  
 370 to study the detector performance in different regimes. Higher voltage is  
 371 expected to enhance the initial avalanche, thus increase the smaller charge  
 372 spreading signal as well. Signals in the neighbour pads are then more likely to  
 373 pass above the threshold and are less affected by statistical fluctuations. As  
 374 track position reconstruction relies on the charge spreading measurements  
 375 we expect better performance with higher voltage. The results are shown  
 376 in Figure 9 (b).

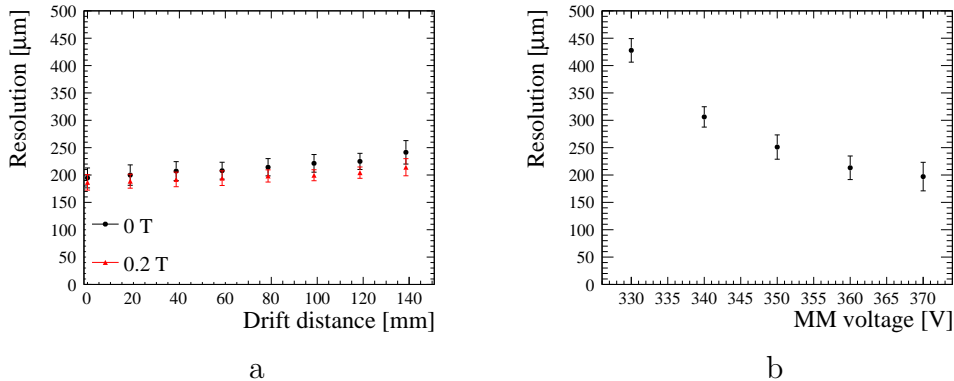


Figure 9: Spatial resolution with respect to (a) beam injection position and (b) Micromegas voltage (DLC voltage) for horizontal tracks parallel to the MM plane. Points represent the mean value over detector columns and errors represent the fluctuations (RMS).

377 The DESY beamline allows changing the momentum of the electrons  
 378 delivered to the test beam area. In this way, we studied spatial resolution  
 379 as a function of the track kinematics. We find no significant changes for the  
 380 position accuracy reconstruction for the tracks in the range between 1 and 5  
 381 GeV/c (Figure 10).

#### 382 7.4. Spatial resolution dependence on the track inclination

383 Tracks inclined with respect to pad borders are expected to be recon-  
 384 structed less precisely compared to horizontal ones. As an example, in the  
 385 current ND280 TPCs, the resolution degrades as a function of the track angle  
 386 from 600  $\mu\text{m}$  to  $\sim 1$  mm [6]. It is then particularly interesting to investigate

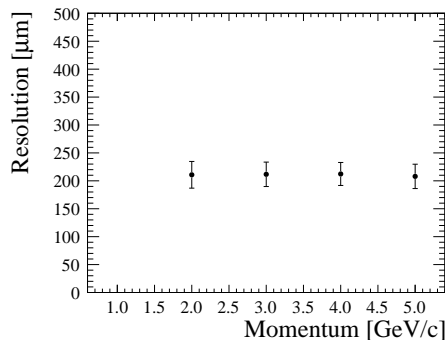


Figure 10: Spatial resolution as a function of the momentum of the electron beam.

387 the behaviour of the spatial resolution in the ERAM detector as a function  
 388 of the angle of the reconstructed track on the ERAM plane with respect to  
 389 the ERAM side (track inclination).

390 In order to do this, the different cluster patterns described in section 5  
 391 were used for different track inclination. The  $\chi^2$  fit (Equation 4) is applied  
 392 to each cluster to extract the track position. As for horizontal tracks, the  
 393 positions in given clusters are fit together to form a global fit and the iterative  
 394 analysis is applied: the barycentric estimation is used as a prior following  
 395 with PRF calibration. The results of the inclined track spatial resolution  
 396 estimations are shown in Figure 11.

397 As expected, the column clustering method leads to a severe spatial res-  
 398 olution degradation with the track slope, reaching a maximum of 1.4 mm  
 399 for 45° tracks. For these angles, the diagonal pattern provides a significant  
 400 performance improvement. In the intermediate regions (20°, 30°, 60°, 70°),  
 401 the best result is achieved with the more complex patterns: “2 by 1” and  
 402 “3 by 1”. The asymmetry with respect to 45° is caused by the rectangular  
 403 pad shape 11.3×10.2 mm. Thus, the diagonal pattern is considered a better  
 404 choice for 48° tracks than for 45° tracks. Hence, tracks inclined with 50° are  
 405 reconstructed more accurately compared to 40° tracks. Similar behavior is  
 406 observed for all the other patterns.

407 By taking the best clustering algorithm we observe a spatial resolution  
 408 better than 600 μm for all the angles. We understand the difference between  
 409 horizontal tracks and inclined tracks as due to the larger effective pad size for  
 410 diagonal clustering and to the rectangular shape of the pads, while diagonal  
 411 clustering would work better for square pads. For a spatial resolution of

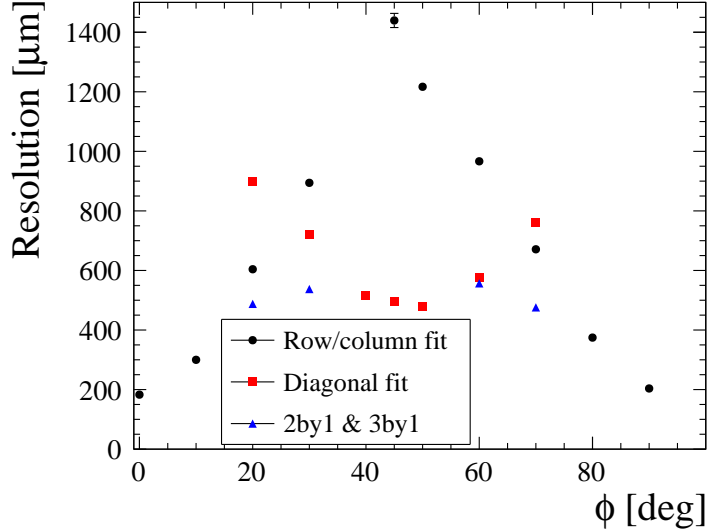


Figure 11: Spatial resolution with respect to track angle within the MM side obtained with different cluster definitions.

412 600  $\mu\text{m}$ , for 70 point measurements and a magnetic field of 0.2 T we expect a  
 413 momentum resolution of 6% at 1 GeV/c that scales linearly with the spatial  
 414 resolution.

#### 415 7.5. Bias measurements

416 As described above, we define the spatial resolution as a standard devi-  
 417 ation of the difference between the reconstructed position in a given cluster  
 418 and a global track fit. Meanwhile, the mean value of the residuals is also an  
 419 important characteristic that shows the bias of our measurements. In par-  
 420 ticular, it is interesting to study the biases with respect to the track position  
 421 in the pad. For that, we use the natural beam spread. The electron beam  
 422 profile is nearly Gaussian with a standard deviation  $\approx 1$  cm. We sample  
 423 the residuals with the reconstructed track position in the pad. Thus, we can  
 424 study the resolution and biases in the different pad regions. In Figure 12, we  
 425 show both the spatial resolution and bias per column. Individual PRFs were  
 426 used for each column to analyze the behaviour in the different regions of the  
 427 detector independently. The resolution undergoes some oscillations because  
 428 if a track is close to one of the leading pad borders, the neighbouring pads

429 see a larger signal and we thus have a more reliable input for the position  
 430 reconstruction.

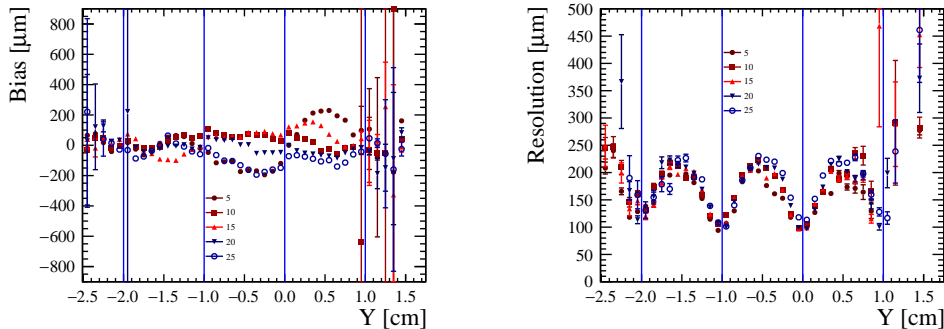


Figure 12: The resolution and the bias of the track reconstruction over the position in the pad for various columns (represented in legend). The pad borders are represented with vertical lines. In this coordinate system, the beam is centred around  $Y = -0.5\text{cm}$ , but tracks are also measured on the neighbour pads due to the beam spread.

431 We generalize the bias study for the whole detector. Figure 13 represents  
 432 the fluctuations of the resolution and biases in the given column. We con-  
 433 clude that for most of the detector the biases are under control and smaller  
 434 compared to the spatial resolution. In the downstream part of the detector,  
 435 we found larger biases that could be related to the non-uniformities in the  
 436 resistivity of this ERAM detector that will be described in section 9.

## 437 8. Deposited energy resolution

438 One of the main goals of a TPC is to perform particle identification (PID)  
 439 based on the measurement of the ionization produced by charged particles  
 440 crossing the gas volume. The PID capabilities depend on the resolution in  
 441 the ionization energy loss measurements.

442 In the case of T2K TPCs, the PID is mainly used to distinguish electrons  
 443 (produced by  $\nu_e$ ) from muons (produced by  $\nu_\mu$ ). In the momentum range  
 444 studied by T2K, the amount of ionization between electrons and muons differs  
 445 by  $\sim 40\%$ . Therefore, a resolution of less than 10% allows to efficiently  
 446 distinguish these two particles. In general, the resolution depends on the  
 447 number of independent ionization measurements (i.e. the number of clusters)  
 448 and on the amount of ionization in each cluster. For the existing TPCs, a

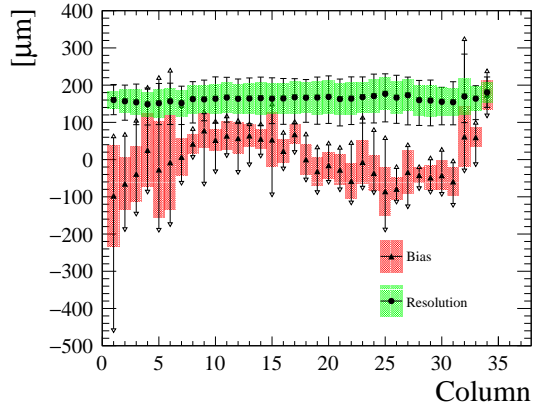


Figure 13: The spatial resolution and bias fluctuations observed for the different positions of the track in the pad. Dots represent the mean value in a given column, filled areas correspond to the RMS, and error bars represent minimum and maximum values.

449 resolution of 8% was obtained by combining measurements in 2 Micromegas  
 450 detectors (72 independent measurements of ionization).

451 In this section, we will describe the performances observed with one single  
 452 ERAM detector ( $36 \times 32$  pads).

453 The method used to estimate the energy loss of a given track is called the  
 454 truncated mean method: the charges contained in each cluster of the track are  
 455 sorted by increasing order and only a fraction of the lowest charged clusters  
 456 is kept to compute the mean deposited energy per track. Such a method  
 457 allows to reject clusters with a large amount of charge, due to fluctuations in  
 458 the ionization processes, which would degrade the relative resolution on the  
 459 mean value, and thus the power to separate different types of particles.

460 The dependence of the  $dE/dx$  resolution for the tracks parallel to the pad  
 461 size on the truncation fraction is shown in Figure 14. The best resolution is  
 462 obtained for values of truncation fraction between 50% and 80%. Therefore,  
 463 for all the results presented in this section, a truncation factor of 70% is used.

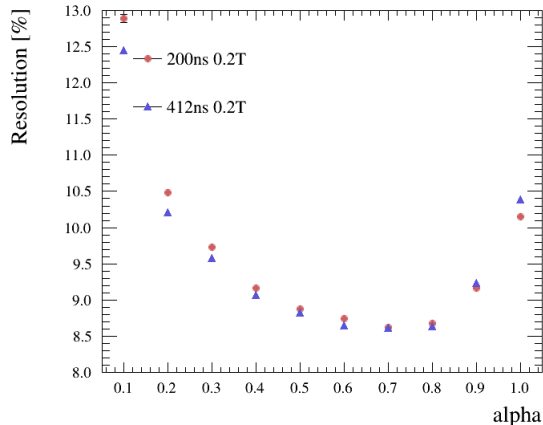


Figure 14: The dependence of the  $dE/dx$  resolution on the truncation factor  $\alpha$  for the beam parallel to the pad sides with a magnetic field of 0.2 T and electronics peaking times of either 200 ns and 412 ns

#### 464 8.1. Definition of the cluster charge

465 As explained before, the basic ingredient of the  $dE/dx$  resolution is the  
 466 amount of charge seen in each cluster. This quantity can be defined in  
 467 different ways.

468 In the existing ND280 TPCs or in the results published in [10], the clus-  
 469 ter charge is defined by summing the waveform maximum seen in each pad  
 470 composing the cluster. This definition was shown to be a good estimator of  
 471 the charge in the case of bulk Micromegas, or when the drift distance is large  
 472 enough to allow the predominance of transverse diffusion over the charge  
 473 spreading induced in the ERAM module.

474 However, in the present configuration, the limited size of the TPC implies  
 475 that the transverse diffusion is small and that charge spreading dominates,  
 476 except when the track is close to the pad border. Therefore, by summing  
 477 the maximum of the waveform seen in each pad of the cluster, we are over  
 478 counting the leading pad charge: first, it is seen in the leading pad before  
 479 the spread, and then seen by the neighboring pads after the spread.

480 To remove this over counting effect, the charge per cluster can be defined  
 481 in a different way. For each cluster, we build a summed waveform defined  
 482 as the sum of the waveform amplitude seen in each pad of the cluster at  
 483 all times. We then take as a cluster charge estimator the maximum of this  
 484 summed waveform. We refer to this method as  $WF_{sum}$ .

485 A comparison of the results of the two methods as a function of the drift  
 486 distance is shown in Figure 15 for the two different peaking times and for data  
 487 taken with 0.2 T magnetic field and with the beam parallel to the ERAM  
 488 side. It can be seen that with both methods, the resolution is well below  
 489 10% for all the drift distances and, as expected, the  $WF_{sum}$  method gives a  
 490 better resolution comprised between 8.5% and 9.0%.

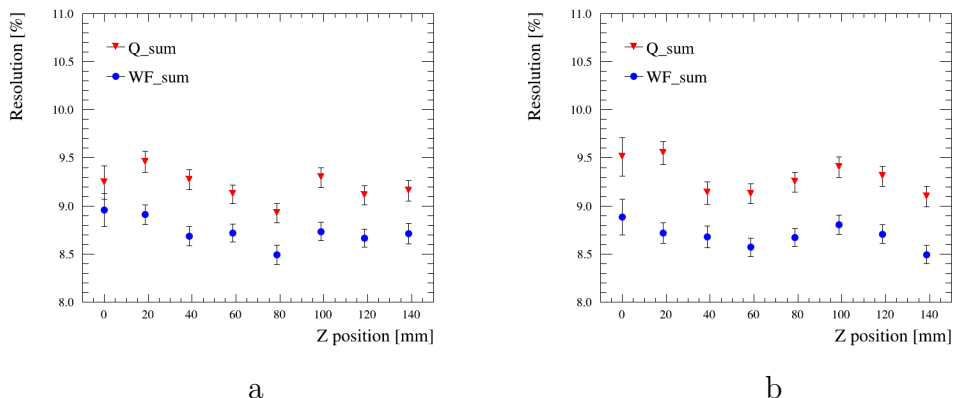


Figure 15:  $dE/dx$  resolution with respect to the drift distance for the beam parallel to the pad side with a magnetic field of 0.2 T and peaking times of 200 ns (a) and 412 ns (b).  $Q_{sum}$  method consists in summing the maximum of the waveform in each pad of the cluster while  $WF_{sum}$  corresponds to the maximum of the summed waveforms in a cluster.

### 491 8.2. Deposited energy resolution for inclined tracks

492 As explained in section 5, in order to reconstruct inclined tracks, different  
 493 clustering algorithms are used. In the case of the deposited energy resolution,  
 494 the usage of such algorithms has two impacts: a larger number of clusters  
 495 per track are reconstructed but the track will have different paths in different  
 496 clusters.

497 In the column or row clusters (defined in Figure 6), tracks with the same  
 498 angle with respect to the pad sides have the same  $dx$  in each cluster (ne-  
 499 glecting the curvature induced by the magnetic field). This is not true for  
 500 diagonal clusters in which the  $dx$  can vary between 0 and the diagonal of the  
 501 pad ( $\sim 1.5$  cm). The distribution of the charge as a function of  $dx$  for tracks  
 502 inclined by 45 degrees with respect to the pad plane is shown in Figure 16.  
 503 It is clear from this figure that there is a dependence, although this depen-  
 504 dence is not linear as one would expect from the simple consideration that  
 505 the deposited energy should be proportional to the path.



506 The non-linearity is due to the fact that each cluster sees not only the  
 507 direct charge due to the primary ionization, but it also sees some charge due  
 508 to the spread on the resistive plane and to the transverse diffusion in the gas.

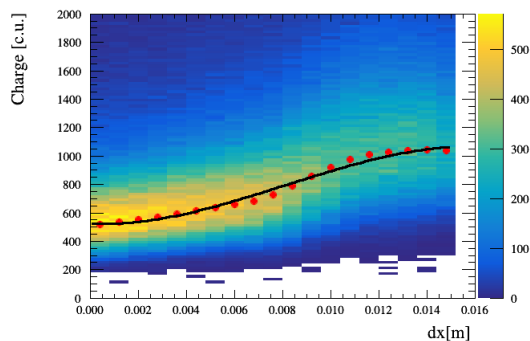


Figure 16: The distribution of the charge with respect to the  $dx$  of the track inclined by 45 degrees with respect to the pad plane. The points represent the most probable value from the fit of the vertical slice with Landau function.

509 In order to correct the  $dx$  in each cluster, we fit the charge in each slice  
 510 of  $dx$  with a Landau function and we take the Most Probable Value (MPV).  
 511 The distribution of MPV as a function of  $dx$  is then parametrized with a  
 512 third degree polynomial. In each cluster, the charge is corrected to take into  
 513 account the real path length  $dx$  and then the truncated mean is computed.

514 The  $dE/dx$  distributions for diagonal clustering with and without the  $dx$   
 515 correction are shown in Figure 17.

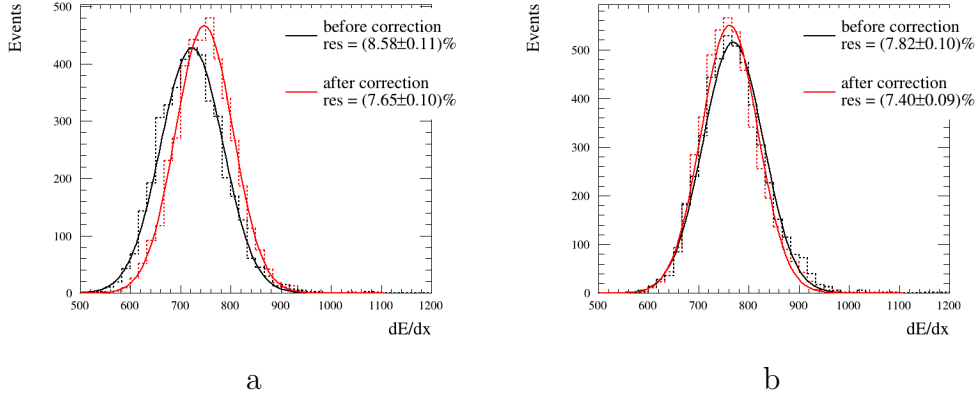


Figure 17: The  $dE/dx$  distribution for 40 deg inclined tracks at an electronics peaking time of 200 ns (a) and 412 ns (b) with and without the correction for  $dx$ .

516 The deposited energy resolution as a function of the beam inclination with  
 517 respect to the pad plane is shown in Figure 18. As expected, the diagonal  
 518 clustering, after proper  $dx$  correction, provides the best resolution thanks to  
 519 the larger amount of clusters in which the track is sampled.

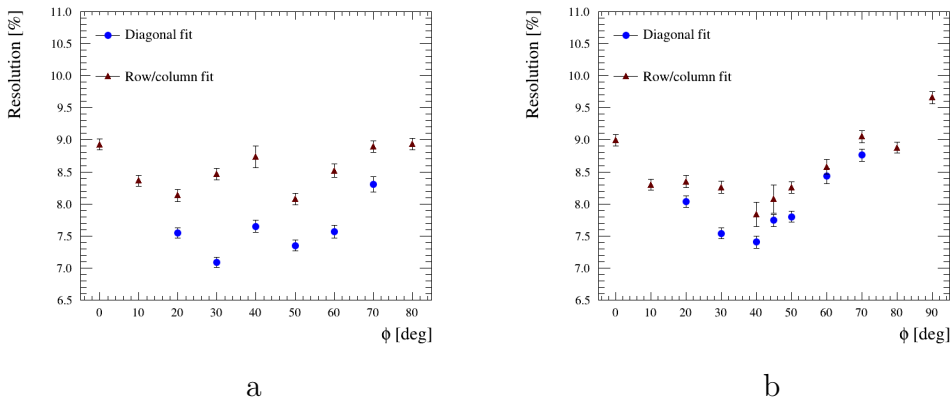


Figure 18:  $dE/dx$  resolution versus the angle with respect to the pad plane using column/row clustering or diagonal clustering. Column clustering is used from 0 to 40 deg and after 40 deg row clustering is used. Runs at a peaking time of 200 ns (a) and 412 ns (b), with a magnetic field of 0.2 T applied to the TPC prototype. Diagonal clustering is corrected for the  $dx$  as described in the text.

520 8.3. Dependence of the  $dE/dx$  resolution on the number of clusters

521 In this test beam, only one ERAM module was used. In the HA-TPC  
 522 that will be installed at ND280, most of the tracks will cross two ERAM  
 523 modules before exiting the TPC resulting in a larger number of clusters  
 524 (72 for tracks parallel to the pad plane). The observed dependence of the  
 525 deposited energy on the number of clusters can then be used to extrapolate  
 526 the expected resolution in the HA-TPCs.

527 This can be done by computing the truncated mean using only a fraction  
 528 of the available clusters. The dependence of the truncated mean on the  
 529 number of clusters used for different samples is shown in Figure 19.

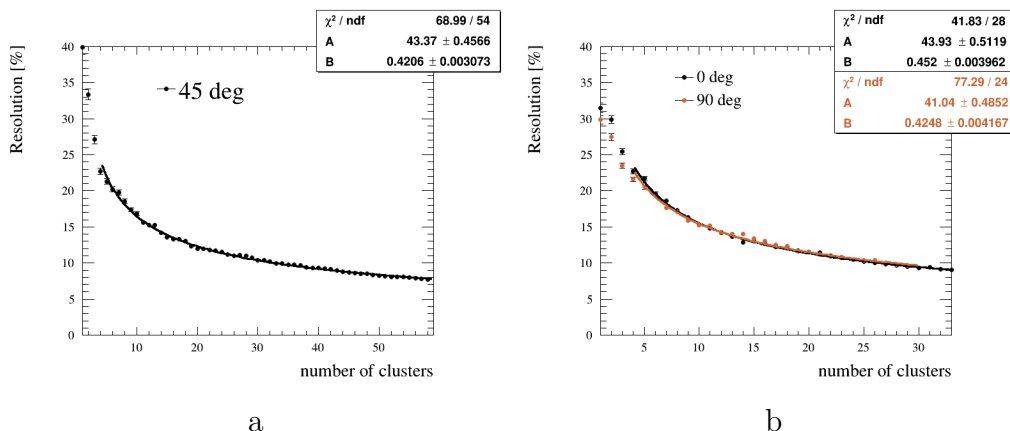


Figure 19:  $dE/dx$  resolution versus the number of clusters for runs at a peaking time of 412 ns with a magnetic field of 0.2T applied to the TPC prototype. Diagonal clustering (including  $dx$  correction) is used for 45 deg inclined tracks (a). In (b), column clustering is employed for 0 deg horizontal tracks and row clustering for 90 deg vertical tracks (b).

530 The resulting distribution of the deposited energy resolution as a function  
 531 of the number of clusters  $N$  is then fit with the function:  $f(N) = AN^{-B}$ .  $B$   
 532 equal to 0.5 would correspond to a simple  $\sqrt{N}$  dependence.

533 In the case of horizontal or vertical tracks, we observe similar behavior:  
 534 the horizontal tracks being slightly better because of the larger pad size in  
 535 the horizontal direction. Extrapolated to two ERAM modules, we obtain a  
 536 deposited energy resolution of the order of 6% for all the angles.

537 **9. RC map calculation**

538 The quantity controlling the charge spreading over time is the product  $RC$   
 539 (section 2. To have a better understanding of our detector, we reconstruct  
 540 the map of  $RC$  using horizontal tracks in data where a scan in y-direction  
 541 was performed at a peaking time of 412 ns. This map is crucial to character-  
 542 ize our detector and its uniformity and is also needed for a detailed detector  
 543 simulation of the electronics response.

544 To extract these  $RC$  values, we use an analytical model of the charge disper-  
 545 sion, adjusted to the waveforms measured in the pads. The induced charge on  
 546 a rectangular pad below the resistive layer can be calculated by integrating  
 547 the charge density function over the pad area [19] :

$$\mathcal{Q}(t) = \frac{q_e}{4} \left[ \operatorname{erf}\left(\frac{x_{\text{high}} - x_0}{\sqrt{2}\sigma(t)}\right) - \operatorname{erf}\left(\frac{x_{\text{low}} - x_0}{\sqrt{2}\sigma(t)}\right) \right] \times \quad (5)$$

$$\left[ \operatorname{erf}\left(\frac{y_{\text{high}} - y_0}{\sqrt{2}\sigma(t)}\right) - \operatorname{erf}\left(\frac{y_{\text{low}} - y_0}{\sqrt{2}\sigma(t)}\right) \right]$$

548 with  $q_e$  is the initial charge,  $(x_0, y_0)$  the track position,  $x_{\text{high}}$ ,  $x_{\text{low}}$ ,  $y_{\text{high}}$ ,  $y_{\text{low}}$   
 549 the pad boundaries. In the denominator  $\sigma(t) = \sqrt{(2t/\tau) + \omega^2}$ , the term  
 550  $\tau = RC$  where  $R$  is the surface resistivity of the layer and  $C$  the capacitance  
 551 determined by the spacing between the anode and readout planes. Finally,  
 552  $\omega$  is associated to the transverse diffusion term.

553

554 To compare to data, the characteristics of the front-end charge pream-  
 555 plifiers need also to be included. Longitudinal diffusion increases the size of  
 556 electron charge clusters in the drift direction. The longitudinal diffusion is  
 557 neglected here since we have only 15 cm drift distance. The parameterization  
 558 of the electronics shaping time effects  $\mathcal{I}(t)$  is obtained from the simulation.  
 559 The convolution of  $\mathcal{I}(t)$  and  $\mathcal{Q}(t)$  results in the full theoretical model, which  
 560 is compared to the data. This convolution is handled numerically. The fit is  
 561 based on clusters of pads perpendicular to the track. Each cluster consists of  
 562 a so-called leading pad collecting essentially the initial charge deposit, and  
 563 in so-called neighbour pads sensitive mostly to the induced charge due to the  
 564 resistive effect, as shown in Figure 4.

565 The fit procedure is as follows: we first fit the leading pad waveform with  
 566 the electronics response function  $\mathcal{I}(t)$ , then we fit simultaneously the two  
 567 neighbouring pads waveform with a convolution of  $\mathcal{I}(t)$  with  $\mathcal{Q}(t)$  in order to

568 extract  $RC$ . Then a simultaneous fit of two neighbouring pads waveform use  
569 separate  $Q(t)$  functions, as the distance to the track can be different for the  
570 two pads, but we consider  $RC$  and the electronics response parameters as  
571 common in the fit. Since we are using horizontal tracks, we can only fit the  
572  $y_0$ -position of the track and we do not have any constraints on its  $x$ -position.  
573 The track position  $y_0$  is obtained with the PRF  $\chi^2$  minimization method (see  
574 equation (4)). Figure 20 shows an example of waveform fit results for the  
leading pad and its neighbours.

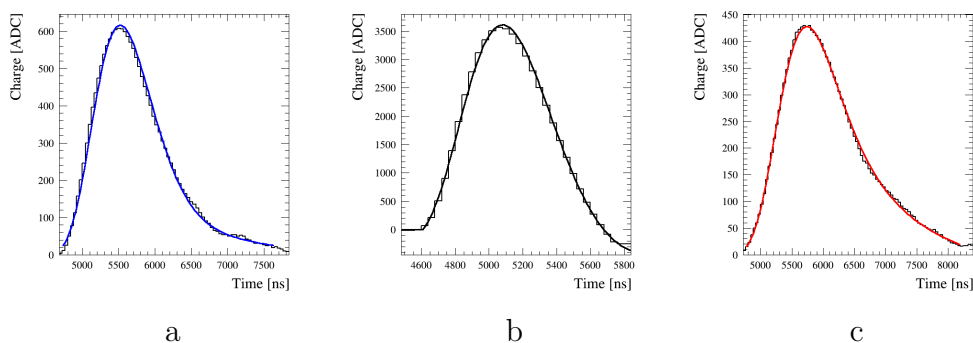


Figure 20: Example of waveform fit results for the leading pad (b) and its neighbors (a) and (c) in a given cluster.

575  
576 Another method can be used to cross-check the  $RC$  values obtained with  
577 the analytical model. This alternative method studies two parameters related  
578 to the signal propagation: the time at which the signal in neighbour  
579 pads is maximal and the ratio of amplitudes of the neighbour pads and the  
580 leading pad. The time difference between the leading pad and one of its  
581 neighbour pads is found to be proportional to  $RC$  as can be seen in the fol-  
582 lowing formula:  $\Delta t_1 - \Delta t_2 = RC \times L \times y_0$ , with  $L$  the pad length and  $y_0$  the  
583 track position and  $\Delta t_{1,2} = t_{\text{Leading Pad}} - t_{\text{Neighbor}}$  the time difference between  
584 the leading pad and the neighbor pad.

585  
586 The  $RC$  maps obtained using the analytical model and the time difference  
587 method described above are shown in Figure 21. The  $RC$  values are given in  
588 unit of  $\text{ns}/\text{mm}^2$ . Both methods give results of the same order of magnitude  
589 although the second method is less precise than the fit procedure. A non-  
590 uniformity of  $RC$  up to 30% is observed using both methods.

591 This non-uniformity is confirmed with the observation of the charge col-

592 lected in the second to leading pad. The charge observed in the leading  
 593 pad is uniform across the detector while the measurements in the neighbours  
 594  $Q_{\text{second}}/Q_{\text{leading}}$  demonstrate fluctuations, especially in the downstream de-  
 595 tector region (Figure 22). The lower charge fraction is consistent with the  
 596 higher  $RC$  value.

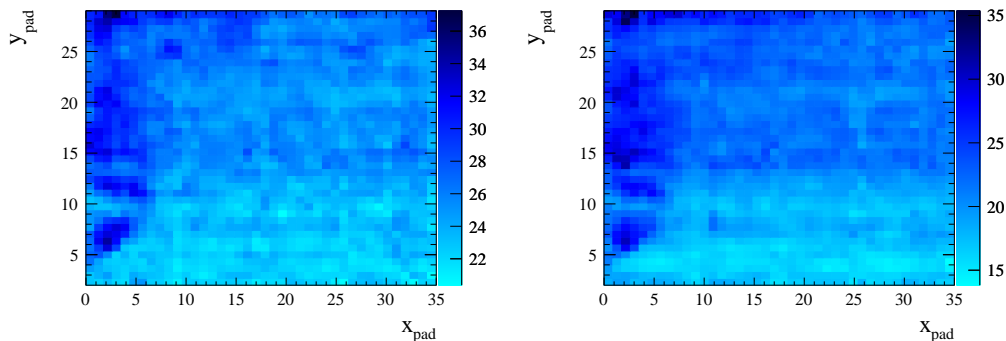


Figure 21: The  $RC$  ( $\text{ns}/\text{mm}^2$ ) map obtained using the fit from the analytical model (left) and the time difference method (right) described in the text.

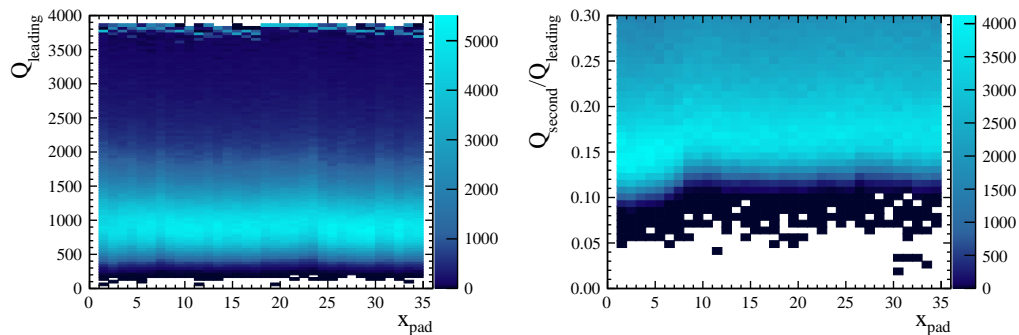


Figure 22: The distribution of the charge in the leading pad (left) and the charge fraction in the second to the leading pad (right) versus the column for horizontal beam tracks.

597 The detector performances such as spatial resolution and  $dE/dx$  resolu-  
 598 tion were studied with the exclusion of the 6 columns where the largest  $RC$   
 599 non-uniformity were observed. No improvement in the detector charac-  
 600 teristics was found. Thus the effect was considered as sub-leading in the detector  
 601 performance limitation.

## 602 **10. Conclusions**

603 We measured the performance of the ERAM prototype with beam parti-  
604 cles at DESY. We studied both spatial and  $dE/dx$  resolution as a function  
605 of the angle of the track with respect to the ERAM plane. We also charac-  
606 terized charge spreading and produced a RC map of the prototype.  
607 Spatial resolution better than 600  $\mu\text{m}$  is obtained for all the angles using  
608 a dedicated clustering algorithm which is adapted to the track angle. En-  
609 ergy resolution better than 9% is obtained for all the angles. We expect  
610 ionization energy loss resolution to be better than 7% for tracks crossing two  
611 ERAMs. Such performances fully satisfy the requirements for the upgrade  
612 of the ND280 TPC.

## 613 **Acknowledgements**

614 The measurements leading to these results have been performed at the  
615 Test Beam Facility at DESY Hamburg (Germany), a member of the Helmholtz  
616 Association. The authors would like to thank the technical team at the DESY  
617 II accelerator and test beam facility for the smooth operation of the test beam  
618 and the support during the test beam campaign.

619 We acknowledge the support of CEA and CNRS/IN2P3, France; DFG, Ger-  
620 many; INFN, Italy; National Science Centre (NCN) and Ministry of Science  
621 and Higher Education (Grant No. DIR/WK/2017/05), Poland; MINECO  
622 and ERDF funds, Spain.

623 In addition, participation of individual researchers and institutions has been  
624 further supported by H2020 Grant No. RISE-GA822070-JENNIFER2 2020,  
625 MSCA-COFUND-2016 No.754496, ANR-19-CE31-0001, RFBR grants #19-  
626 32-90100, the Ministry of Science and Higher Education of Russia (contract  
627 #075-15-2020-778) the Spanish Ministerio de Economía y Competitividad  
628 (SEIDI - MINECO) under Grants No. PID2019-107564GB-I00 and SEV-  
629 2016-0588. IFAE is partially funded by the CERCA program of the Gener-  
630 alitat de Catalunya.

## 631 **References**

- 632 [1] K. Abe, et al., The T2K Experiment, Nucl. Instrum. Meth. A659 (2011)  
633 106–135. arXiv:1106.1238, doi:10.1016/j.nima.2011.06.067.

- 634 [2] K. Abe, et al., Indication of Electron Neutrino Appearance from an  
635 Accelerator-produced Off-axis Muon Neutrino Beam, *Phys. Rev. Lett.*  
636 107 (2011) 041801. [arXiv:1106.2822](#), [doi:10.1103/PhysRevLett.](#)  
637 [107.041801](#).
- 638 [3] K. Abe, et al., Evidence of Electron Neutrino Appearance in a Muon  
639 Neutrino Beam, *Phys. Rev. D* 88 (3) (2013) 032002. [arXiv:1304.0841](#),  
640 [doi:10.1103/PhysRevD.88.032002](#).
- 641 [4] K. Abe, et al., Observation of Electron Neutrino Appearance in a Muon  
642 Neutrino Beam, *Phys. Rev. Lett.* 112 (2014) 061802. [arXiv:1311.4750](#),  
643 [doi:10.1103/PhysRevLett.112.061802](#).
- 644 [5] K. Abe, et al., Constraint on the matter–antimatter symmetry-violating  
645 phase in neutrino oscillations, *Nature* 580 (7803) (2020) 339–344, [Er-  
646 ratum: *Nature* 583, E16 (2020)]. [arXiv:1910.03887](#), [doi:10.1038/](#)  
647 [s41586-020-2177-0](#).
- 648 [6] N. Abgrall, et al., Time Projection Chambers for the T2K Near De-  
649 tectors, *Nucl. Instrum. Meth. A* 637 (2011) 25–46. [arXiv:1012.0865](#),  
650 [doi:10.1016/j.nima.2011.02.036](#).
- 651 [7] K. Abe, et al., Measurement of the intrinsic electron neutrino component  
652 in the T2K neutrino beam with the ND280 detector, *Phys. Rev. D* 89  
653 (2014) 092003. [arXiv:1403.2552](#), [doi:10.1103/PhysRevD.89.092003](#).
- 654 [8] K. Abe, et al., Measurement of the charged-current electron (anti-  
655 )neutrino inclusive cross-sections at the T2K off-axis near detector  
656 ND280, *JHEP* 10 (2020) 114. [arXiv:2002.11986](#), [doi:10.1007/](#)  
657 [JHEP10\(2020\)114](#).
- 658 [9] A. Blondel, M. Bogomilov, S. Bordini, F. Cadoux, D. Douqa, K. Dugas,  
659 T. Ekelof, Y. Favre, S. Fedotov, K. Fransson, R. Fujita, E. Gramstad,  
660 A. Ichikawa, S. Ilieva, K. Iwamoto, C. Jesús-Valls, C. Jung, S. Kasetti,  
661 M. Khabibullin, A. Khotjantsev, A. Korzenev, A. Kostin, Y. Kudenko,  
662 T. Kutter, T. Lux, L. Maret, T. Matsubara, A. Mefodiev, A. Minamino,  
663 O. Mineev, G. Mitev, M. Nessi, L. Nicola, E. Noah, S. Parsa, G. Petkov,  
664 F. Sanchez, D. Sgalaberna, W. Shorrock, K. Skwarczynski, S. Suvorov,  
665 A. Teklu, R. Tsenov, Y. Uchida, G. Vankova-Kirilova, N. Yershov,



- 666 M. Yokoyama, J. Zalipska, Y. Zou, W. Zurek, The SuperFGD proto-  
667 type charged particle beam tests, *Journal of Instrumentation* 15 (12)  
668 (2020) P12003–P12003. doi:10.1088/1748-0221/15/12/p12003.  
669 URL <https://doi.org/10.1088/1748-0221/15/12/p12003>
- 670 [10] D. Attié, et al., Performances of a resistive Micromegas module for  
671 the Time Projection Chambers of the T2K Near Detector upgrade,  
672 *Nucl. Instrum. Meth. A* 957 (2020) 163286. arXiv:1907.07060, doi:  
673 10.1016/j.nima.2019.163286.
- 674 [11] K. Abe, et al., T2K ND280 Upgrade - Technical Design Report (2019).  
675 arXiv:1901.03750.
- 676 [12] I. Giomataris, R. De Oliveira, S. Andriamonje, S. Aune, G. Charpak,  
677 P. Colas, A. Giganon, P. Rebourgeard, P. Salin, Micromegas in a bulk,  
678 *Nucl. Instrum. Meth. A* 560 (2006) 405–408. arXiv:physics/0501003,  
679 doi:10.1016/j.nima.2005.12.222.
- 680 [13] M. S. Dixit, J. Dubeau, J. P. Martin, K. Sachs, Position sensing from  
681 charge dispersion in micropattern gas detectors with a resistive anode,  
682 *Nucl. Instrum. Meth. A* 518 (2004) 721–727. arXiv:physics/0307152,  
683 doi:10.1016/j.nima.2003.09.051.
- 684 [14] R. Diener, et al., The DESY II Test Beam Facility, *Nucl. Instrum.*  
685 *Meth. A* 922 (2019) 265–286. arXiv:1807.09328, doi:10.1016/j.  
686 nima.2018.11.133.
- 687 [15] M. Ester, H.-P. Kriegel, J. Sander, X. Xu, A density-based algorithm for  
688 discovering clusters in large spatial databases with noise, in: *Proceedings*  
689 *of the Second International Conference on Knowledge Discovery and*  
690 *Data Mining*, AAAI Press, 1996, pp. 226–231.
- 691 [16] R. Gluckstern, Uncertainties in track momentum and direc-  
692 tion, due to multiple scattering and measurement errors, *Nu-*  
693 *clear Instruments and Methods* 24 (1963) 381–389. doi:[https://doi.org/10.1016/0029-554X\(63\)90347-1](https://doi.org/10.1016/0029-554X(63)90347-1).  
694 URL <https://www.sciencedirect.com/science/article/pii/0029554X63903471>  
695  
696
- 697 [17] D. Attie, Beam tests of Micromegas LC-TPC large prototype, *JINST* 6  
698 (2011) C01007. doi:10.1088/1748-0221/6/01/C01007.

- 699 [18] K. Boudjemline, M. S. Dixit, J. P. Martin, K. Sachs, Spatial resolution of  
700 a GEM readout TPC using the charge dispersion signal, Nucl. Instrum.  
701 Meth. A574 (2007) 22–27. [arXiv:physics/0610232](https://arxiv.org/abs/physics/0610232), [doi:10.1016/j.](https://doi.org/10.1016/j.nima.2007.01.017)  
702 [nima.2007.01.017](https://doi.org/10.1016/j.nima.2007.01.017).
- 703 [19] M. S. Dixit, J. Dubeau, J. P. Martin, K. Sachs, Position sensing from  
704 charge dispersion in micropattern gas detectors with a resistive anode,  
705 Nucl. Instrum. Meth. A518 (2004) 721–727. [arXiv:physics/0307152](https://arxiv.org/abs/physics/0307152),  
706 [doi:10.1016/j.nima.2003.09.051](https://doi.org/10.1016/j.nima.2003.09.051).